

# GeV $\gamma$ -ray emission in the low-mass star-forming region AFGL 490

Li-Nuo Yang,<sup>1</sup> Sheng Tang,<sup>1</sup> Pak-Hin Thomas Tam,<sup>1,2\*</sup>

<sup>1</sup>*School of Physics and Astronomy, Sun Yat-sen University, Zhuhai 519082, China*

<sup>2</sup>*CSST Science Center for the Guangdong-Hong Kong-Macau Greater Bay Area, Sun Yat-Sen University, Zhuhai 519082, China*

Accepted XXX. Received YYY; in original form ZZZ

## ABSTRACT

We report the discovery of an extended GeV  $\gamma$ -ray source, 4FGL J0330.7+5845e, associated with the star-forming region AFGL 490 using 17 years of *Fermi*-LAT data. The emission is spatially coincident with a dense molecular cloud and centered near the massive protostar AFGL 490. Its spectral energy distribution shows a distinct high-energy cutoff. Both leptonic and hadronic models can fit the  $\gamma$ -ray spectrum, but energetic arguments rule out stellar winds as the primary accelerator. Instead, the protostellar jet driven by AFGL 490 is identified as a plausible site for particle acceleration, and the derived timescales and maximum particle energies are consistent with theoretical predictions for such jets.

**Key words:** gamma rays: ISM – ISM: individual: AFGL 490 – cosmic rays – stars: jets – acceleration of particles

## 1 INTRODUCTION

Star-forming (SF) regions, which are often observed to be embedded in giant molecular clouds (GMCs), provide excellent environments for studying particle acceleration. The existence of many massive OB stars (sometimes including Wolf-Rayet stars) within a small volume can form young massive clusters (YMC). The intense radiation pressure from the massive stars can drive strong stellar winds with terminal velocity up to 3000 km s<sup>-1</sup> (Lucy & Solomon 1970). The combined action of stellar winds from multiple massive stars, together with possible supernova remnants within the cluster, can produce a powerful collective cluster wind. The interaction of this collective outflow with the surrounding interstellar medium can generate large-scale shocks and turbulence, providing favorable conditions for particle acceleration (Bykov et al. 2013; Morlino et al. 2021). YMCs can also sustain high-energy winds over timescales of several million years, fertilizing efficient long-term acceleration of charged particles.

Over the past decade or so, many studies have investigated  $\gamma$ -ray emission from YMC in SF regions including Cygnus Cocoon (Ackermann et al. 2011; Abeyssekara et al. 2021; Lhaaso Collaboration 2024), NGC 3603 (Yang & Aharonian 2017), Westerlund 2 (Yang et al. 2018), W43 (Yang & Wang 2020), W40 (Sun et al. 2020) and RCW 38 (Ge et al. 2024). Typically in the above works,  $\gamma$ -ray emission can be well explained by the colliding stellar winds model.

However, a less-studied scenario also exists: Romero (2010) pointed out that, in addition to collective stellar winds from cluster, protostellar jets could also contribute to  $\gamma$ -ray emission in SF regions. The jets are typically generated during protostellar formation: as the protostar accretes material from the dense GMC in which it is embedded in, it produces jets in which charged particles are accelerated via the Diffusive Shock Acceleration (DSA) mechanism (Bell 1978; Blandford & Ostriker 1978). With velocities ranging from 300 to 1500 km s<sup>-1</sup> (Araudo et al. 2021), the high-speed jet

termination collides with the surrounding dense medium, and  $\gamma$  rays are mainly produced through relativistic Bremsstrahlung and proton-proton ( $pp$ ) collisions (Bosch-Ramon et al. 2010). The latter process generates  $\pi^0$  mesons (decaying into  $\gamma$  rays) as well as charged pions ( $\pi^+/\pi^-$ ). The subsequent decay of  $\pi^+/\pi^-$  produces secondary electrons/positrons, which can be further accelerated to emit synchrotron radiation. Along this line, Araudo et al. (2007, 2021) and Bosch-Ramon et al. (2010) have developed the model for  $\gamma$ -ray emission from protostellar jets and placed constraints on the parameters of the jets. Recent studies also suggest that protostars with jets are GeV  $\gamma$ -ray sources and provide excellent laboratories for investigating particle acceleration mechanisms (Yan et al. 2022; de Oña Wilhelmi et al. 2023; Méndez-Gallego et al. 2025).

The SF region AFGL 490, as recognized as an embedded cluster of low-mass Young Stellar Objects (YSOs) around the high-mass (8 – 10  $M_{\odot}$ ) protostar AFGL 490 (Straizys & Laugalys 2008; Masiunas et al. 2012), is located at a distance of approximately 1.0 kpc (Snell et al. 1984; Straizys & Laugalys 2008) within the plane of the Galaxy in the Cam OB1 association. In fact, the protostar AFGL 490 resides within a locally over-dense cluster core containing 219 identified YSOs, which are estimated to be around 10<sup>6</sup> years old with an average mass of about 0.5  $M_{\odot}$  (Masiunas et al. 2012). The protostar AFGL 490 itself has a bolometric luminosity of 2000  $L_{\odot}$  (Schreyer et al. 2006) and an estimated age of 10<sup>4</sup> – 10<sup>5</sup> years (Schreyer et al. 2002). Furthermore, multiwavelength observations have revealed its detailed structure, which comprises a prominent bipolar molecular jet (Snell et al. 1984; Navarete et al. 2015), an extended envelope (Schreyer et al. 2002), and a rotating disk (Schreyer et al. 2006). The protostar AFGL 490 has also been observed to have two non-thermal radio lobes (Obonyo et al. 2019) similar to HH objects, which confirms the presence of synchrotron radiation, implying the existence of charged particles at relativistic speeds. Based on the position of these non-thermal radio lobes as the termination point of the protostellar jet (Bosch-Ramon et al. 2010), the jet radius can be inferred to be  $R_j \sim 4.5 \times 10^{16}$  cm.

\* E-mail: tanbxuan@sysu.edu.cn

In this paper, we analysed 17 years of *Fermi*-LAT data to understand the origin of the  $\gamma$ -ray emission around the SF region AFGL 490. The paper is organized as follows. In Sect. 2, we present the data processing procedure for the  $\gamma$ -ray observations. In Sect. 3, we study the gas distribution in this region. In Sect. 4, we test both leptonic and hadronic models to describe the  $\gamma$ -ray emission. The results of our discussion are presented in Sect. 5, and the final conclusions are summarized in Sect. 6.

## 2 FERMI-LAT DATA ANALYSIS

The Fermi Large Area Telescope (*Fermi*-LAT) is a space-based gamma-ray observatory capable of surveying a broad energy range from 20 MeV to beyond 1 TeV. The LAT detects  $\gamma$ -rays by measuring the arrival time, energy, and direction of incident photons using its tracker subsystem and calorimeter.

We performed our analysis using *Fermipy* v1.4.0<sup>1</sup>(Wood et al. 2017). The dataset spans the period from 2008 August 6 (Mission Elapsed Time, MET = 239673601) to 2025 August 6 (MET = 776131205). The P8R3\_SOURCE\_V3 instrument response functions (IRFs) were selected for the analysis of events. To maximize the statistical significance, we chose events with `evtype = 3` and `evclass = 128`. Additionally, the recommended quality filter expression (`DATA_QUAL > 0`) && (`LAT_CONFIG == 1`) was applied to select the Good Time Intervals, based on the information provided in the spacecraft file.

Our Region of Interest (ROI) is a  $16^\circ \times 16^\circ$  square centered at the position of the protostar AFGL 490 with Galactic longitude and latitude ( $l = 142.00^\circ$ ,  $b = 1.82^\circ$ ). Additionally, to reduce contamination from Galactic diffuse emission, we selected photons in the 300 MeV–300 GeV energy range for our analysis, following, e.g., (Méndez-Gallego et al. 2025).

### 2.1 Spatial analysis

Within the initial  $3^\circ \times 3^\circ$  region centered on the protostar AFGL 490, we identified five  $\gamma$ -ray sources from the *Fermi*-LAT 4FGL Data Release 4 (DR4) catalog (Abdollahi et al. 2022; Ballet et al. 2023), sorted by their angular offset from the ROI center in ascending order: 4FGL J0330.7+5845 ( $0.403^\circ$ ), 4FGL J0329.2+5750c ( $0.959^\circ$ ), 4FGL J0328.0+6046 ( $1.988^\circ$ ), 4FGL J0323.6+6142 ( $2.970^\circ$ ), and 4FGL J0305.4+5945c ( $2.993^\circ$ ).

For clarity of presentation, we subsequently only show the  $2^\circ \times 2^\circ$  region (see Fig. 1). This refined ROI contains only two catalog sources: 4FGL J0330.7+5845 ( $l = 142.349^\circ$ ,  $b = 2.022^\circ$ ) and 4FGL J0329.2+5750c ( $l = 142.7^\circ$ ,  $b = 1.164^\circ$ ). In the analysis, all spectral parameters of these two sources are left free during the log-likelihood fitting. In addition, we allowed the normalization parameters of all sources within  $5^\circ$  of the ROI center to vary, as well as the normalizations of the Galactic diffuse emission and the isotropic background components.

We conducted a preliminary analysis to delineate the boundaries of the dense core within the AFGL 490 cluster (see Sect. 1) based on the results of Masiunas et al. (2012), whose outline is traced by the cyan irregular polygon in Fig. 1.

<sup>1</sup> <https://fermipy.readthedocs.io/en/latest/>

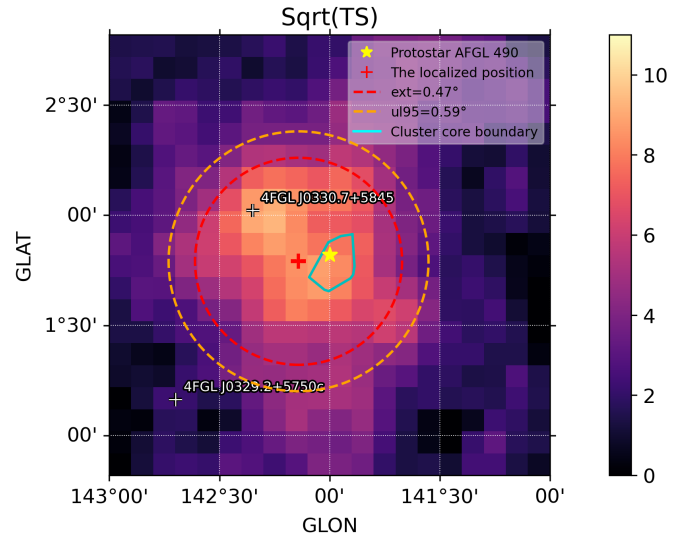


**Figure 1.** Initial(before *localize*) Sqrt(TS) map for a  $2^\circ \times 2^\circ$  region centered on protostar AFGL 490. Only the source 4FGL J0330.7+5845 was excluded, and the spectral index of the test point source was set to be 2.2.

#### 2.1.1 Localize the source 4FGL J0330.7+5845

We initially note the apparent presence of a faint dual-peak structure in Fig. 1, characterized by one TS peak coincident with the known source 4FGL J0330.7+5845 and another located near the protostar AFGL 490. To investigate this, we added a trial point source with a power-law spectrum at the position of AFGL 490. While the fit converged successfully and produced an increase in the global log-likelihood of  $\Delta \log L = 19$ , the trial source itself exhibits a TS value of only 7.7 and an anomalously steep spectral index of  $\sim 5$ . Given these characteristics, the feature is unlikely to represent a genuine astrophysical source. Furthermore, a systematic search for new point sources within a  $2^\circ \times 2^\circ$  region, conducted using the `find_source` method in *Fermipy*, also returned no significant candidates. For a more detailed investigation of this possible two-point-source structure, see Sec. 2.1.3.

We then performed a re-localization of the source 4FGL J0330.7+5845 using the `localize` method in *Fermipy*. The analysis yields an increase of TS from 134.8 to 138.7 and a positional offset of  $0.31^\circ$  from the original catalog position. The refined coordinates are ( $l = 142.14^\circ$ ,  $b = 1.79^\circ$ ), which reduces the angular separation from the protostar to  $0.144^\circ$ . The (re-)localization makes the protostar to lie within the 95% containment radius ( $r_{95} = 0.147^\circ$ ) of the refined  $\gamma$ -ray position, which is marked with a red cross in Fig. 1. We refer to the model incorporating this updated position as Model 1 in the subsequent analysis.

We also attempted to localize the source 4FGL J0329.2+5750c (TS = 37.3) after the localization of 4FGL J0330.7+5845. The localization resulted in a marginal improvement of the fit, with the TS increasing by about 2. The corresponding best-fit position was shifted by only  $0.09^\circ$  relative to the catalog value, indicating no significant positional change. We therefore retained its catalog position for the subsequent analysis.

Additionally, we selected photons using the combinedPSF event type, which jointly includes all four PSF event classes, providing the best angular resolution while preserving sufficient statistics, and performed localization for the source 4FGL J0330.7+5845. The re-

sult was similar to that obtained with `evtype = 3`: the position shifted by  $0.32^\circ$ , with the new position at ( $l = 142.14^\circ$ ,  $b = 1.77^\circ$ ). This position is  $0.149^\circ$  away from the protostar ( $r_{99} = 0.175^\circ$ ). We adopted this new position and refer to the model after localization with combinedPSF events as Model 2 in the subsequent analysis.

### 2.1.2 Extension test for 4FGL J0330.7+5845

We employed the extension method in *Fermipy* to test the spatial extension of 4FGL J0330.7+5845 based on Model 1 and Model 2. This analysis was performed across different energy bins and under various assumptions of the source model to ensure robustness. The method determines the best-fit extension parameters by maximizing the likelihood function. Additionally, we conducted a comparative test using photons of the combinedPSF event class only to evaluate its impact on the measured extension.

The Akaike Information Criterion (AIC) (Akaike 1974) was employed to quantitatively compare and select the better model between the extended source model and the point-source model. AIC is given by the following equation:

$$\text{AIC} = 2k - 2 \ln(L) \quad (1)$$

Where  $k$  is the number of independently adjusted parameters in the model and  $L$  is the maximum value of the likelihood function for the model. The best model is considered to be the one that minimises the AIC value. So, the  $\Delta\text{AIC} = \text{AIC}_{\text{ext}} - \text{AIC}_{\text{ps}}$  is used to compare between extension model and initial point source model. In our study, the Gaussian and Disk models were compared against the point-source Model 1, while the Gaussian (combinedPSF) and Disk (combinedPSF) models were compared against the point-source Model 2. Since the spectral shape (logparabola, see Sect. 2.2) and spatial position were fixed, switching from a point source to an extended source only increases the number of free parameters  $k$  by 1. Additionally, the  $\ln(L)$  values can be directly obtained from the *Fermipy* output.

The results of these analyses are summarized in Tab. 1, where the  $\Delta\text{AIC}$  values were computed using the full energy range of 0.3–300 GeV. To investigate whether the observed spatial extension exhibits an energy dependence, the analysis was additionally performed in two separate energy intervals: 0.3–1 GeV and 1–300 GeV, with both models providing strong and consistent evidence in favor of spatial extension.

### 2.1.3 Re-examining the possible two-point-source structure

We performed additional tests to investigate the possible dual-peak structure. First, we selected photons with energies  $> 1$  GeV, which provide a significantly improved PSF. The corresponding TS map still shows a similar two-peak morphology as in Fig. 1. Using this data set, we applied the `find_sources` method in *fermipy*, adopting an assumed spectral index of 2.2, a TS detection threshold of 16, and a minimum separation of  $0.1^\circ$ . However, no additional source was detected in the vicinity (the nearest newly detected source lies more than  $2.6^\circ$  away).

We then added a point source with a power-law spectrum at the location of the second peak ( $l = 142.1^\circ$ ,  $b = 1.6^\circ$ ) and performed a likelihood fit. Before adding this source, the TS value of 4FGL J0330.7+5845 was 66.3; after the fit, the TS values of the newly added source and 4FGL J0330.7+5845 become 39.6 and 40.8, respectively. The resulting spectral indices of both sources (with 4FGL J0330.7+5845 modeled by a log-parabola) are  $\sim 3.2$ , indicating similarly soft spectra. The comparable TS values and nearly

identical soft spectral indices suggest that the emission is likely produced by the same underlying mechanism, and that the fit is likely redistributing the same photon population rather than revealing two independent emitters.

In addition, we performed a dedicated localization and extension analysis of 4FGL J0330.7+5845 using only photons with energies  $> 1$  GeV, following the same procedure as described above. The best-fit position is found to be ( $l = 142.13^\circ$ ,  $b = 1.73^\circ$ ), with an offset of  $0.159^\circ$  from the protostar AFGL 490 (with  $r_{99} = 0.195^\circ$ ), and a TS value of 74.1. At this location, an extension test was carried out using a Gaussian spatial template, yielding  $\text{TS}_{\text{ext}} = 31.4$ , with a best-fit extension radius of  $0.47^{+0.07}_{-0.06}$  and a 95% upper limit of  $0.59^\circ$ . Furthermore, compared with the manually constructed two-point-source model, the extended-source model is preferred with  $\Delta\text{AIC} = -5.7$ . Combined with the consistent evidence for significant extension across all energy bands (see Tab. 1), these results further support a single extended-source interpretation.

On the other hand, the photon energies in this region are only at the level of a few GeV (see Fig. 4), at which the angular resolution of the *Fermi*-LAT remains limited (e.g.,  $\sim 0.8^\circ$  at  $\sim 1$  GeV), and is therefore insufficient to reliably resolve such a marginal and closely spaced ( $\sim 0.5^\circ$ ) double-source structure. In light of this limitation, together with the evidence presented above, we adopt a single extended-source model for 4FGL J0330.7+5845 in the subsequent analysis, using a Gaussian spatial template as the final model and designating the source as 4FGL J0330.7+5845e. The subsequent analysis was therefore performed using the extension radius of 4FGL J0330.7+5845e derived from the 0.3–300 GeV energy band, which was fitted as  $0.47^\circ$  with a 95% upper limit of  $0.59^\circ$ . Both of these radii are indicated in Fig. 1.

## 2.2 Spectral energy distribution

We initially used the log-parabolic (LP) spectral model of the original point source 4FGL J0330.7+5845 for the source 4FGL J0330.7+5845e, which is expressed as:

$$\frac{dN}{dE} = N_0 \left( \frac{E}{E_b} \right)^{-\alpha - \beta \ln(E/E_b)} \quad (2)$$

Our spectral fitting yielded the following parameter values:  $N_0 = (1.847 \pm 0.170) \times 10^{-12} \text{ MeV}^{-1} \text{ cm}^{-2} \text{ s}^{-1}$ ,  $\alpha = 2.312 \pm 0.112$ ,  $\beta = 0.234 \pm 0.089$ , and  $E_b = 1038 \text{ MeV}$ . Then we tested the spectral curvature of 4FGL J0330.7+5845e using the curvature method in *Fermipy*. The results show that both curved spectral models provide a better fit than a simple power-law model. Specifically, we obtain a curvature test statistic of 8.4 for the LP model and 9.9 for the `PLSuperExpCutoff42` (PLSC), with the latter computed by fixing the high-energy index to 0.667. The difference in fit quality between the LP and PLSC models is not statistically significant; therefore, we retained the LP model for the subsequent analysis. The derived spectrum reveals a significant high-energy turn-over feature.

## 3 GAS CONTENT

We investigated three distinct gas phases—molecular hydrogen ( $\text{H}_2$ ), neutral atomic hydrogen (HI), and ionized hydrogen (HII)—in the vicinity of the star-forming region AFGL 490.

<sup>2</sup> [https://fermi.gsfc.nasa.gov/ssc/data/analysis/scitools/source\\_models.html](https://fermi.gsfc.nasa.gov/ssc/data/analysis/scitools/source_models.html)

**Table 1.** Results of the extension test for 4FGL J0330.7+5845. The source has TS value of 138.7 and 132.7 (combinedPSF) within the 300 MeV–300 GeV energy range. The extension radius and the corresponding 95% confidence level upper limits (UL95) for the four spatial models in the 300 MeV–300 GeV energy range are also reported.  $TS_{\text{ext}}$  denotes the test statistic for the spatial extension hypothesis. A  $|\Delta\text{AIC}| > 5$  provides strong evidence in favor of the model with the lower AIC, while a  $|\Delta\text{AIC}| > 10$  offers conclusive evidence (Liddle 2007; Kulkarni & Desai 2017; Lhaaso Collaboration et al. 2025).

Model	Extension radius / UL95 (°)	$\Delta\text{AIC}$	$TS_{\text{ext}}(0.3\text{--}300\text{ GeV})$	$TS_{\text{ext}}(0.3\text{--}1\text{ GeV})$	$TS_{\text{ext}}(1\text{--}300\text{ GeV})$
Gaussian	$0.47^{+0.08}_{-0.06}/0.59$	-31.0	32.8	22.9	74.2
Disk	$0.45^{+0.05}_{-0.05}/0.54$	-30.1	32.0	20.4	68.8
Gaussian (combinedPSF)	$0.46^{+0.07}_{-0.06}/0.58$	-36.3	38.5	27.3	87.0
Disk (combinedPSF)	$0.46^{+0.05}_{-0.05}/0.54$	-35.1	37.3	24.8	81.0

### 3.1 The H<sub>2</sub> distribution

We utilized <sup>12</sup>CO/<sup>13</sup>CO/C<sup>18</sup>O observational data from the MWISP survey (Su et al. 2019) covering a 4°×4° region centered on the ROI to trace the molecular hydrogen distribution. Through queries of the SIMBAD astronomical database (Wenger et al. 2000) and consideration of cluster distances, we selected the molecular cloud PGCC G142.03+1.73 ( $l = 142.034^\circ, b = 1.728^\circ$ ) (Planck Collaboration et al. 2016b) for CO spectral analysis, as it represents the cloud closest to the protostar AFGL 490 and most likely to be spatially associated with the cluster. To identify velocity peaks, we applied Savitzky-Golay filtering (Savitzky & Golay 1964) to smooth the initial <sup>12</sup>CO spectra, revealing two distinct velocity components (see Fig. 2): Peak 1 at  $-13.7\text{ km s}^{-1}$  (consistent with the reported  $V_{\text{LSR}} = -13.4\text{ km s}^{-1}$  at the position of protostar AFGL 490 (Schreyer et al. 2006)) and Peak 2 at  $-10.5\text{ km s}^{-1}$ . Using the Galactic measurements from Reid et al. (2019), we derived kinematic distances of 1.05 kpc and 0.79 kpc for these two peaks, respectively. We subsequently integrated only Peak 1, which is consistent with the cluster distance, over the velocity range of  $[-16.3, -11.27]\text{ km s}^{-1}$  where the Signal-to-Noise Ratio (SNR)  $> 3$ . Adopting a conversion factor of  $X_{\text{CO}} = 2 \times 10^{20}\text{ cm}^{-2}\text{ K}^{-1}\text{ km}^{-1}\text{ s}$  suggested by Dame et al. (2001) and Bolatto et al. (2013), we obtained the  $N_{\text{H}_2}$  distribution map derived from integration of the spectral data of <sup>12</sup>CO (see Fig. 3). Additionally, we integrated the <sup>13</sup>CO spectra (peak velocity:  $-12.8\text{ km s}^{-1}$ , integration range:  $[-15.4, -9.6]\text{ km s}^{-1}$  with SNR  $> 3$ ) and the C<sup>18</sup>O spectra (peak velocity:  $-12.8\text{ km s}^{-1}$ , integration range:  $[-14.1, -11.6]\text{ km s}^{-1}$  with SNR  $> 3$ ) to generate their respective intensity distribution maps. We then delineated the <sup>13</sup>CO and C<sup>18</sup>O intensity contours at a threshold of 10% of their peak intensities (see Fig. 3). Our analysis reveals a good spatial correspondence between the integrated emission of Peak 1 and both the <sup>13</sup>CO and C<sup>18</sup>O contours. Therefore, we adopted the integration results of Peak 1 for subsequent studies.

### 3.2 The HI distribution

We investigated the neutral hydrogen distribution using the HI4PI (HI4PI Collaboration et al. 2016) 21-cm data cube. To impose the same kinematic constraint as for Peak 1, the HI spectra were integrated over the identical velocity interval  $[-16.3, -11.27]\text{ km s}^{-1}$ . We found the HI brightness temperature reaches  $\sim 80\text{ K}$  at this interval, indicating that the emission is not optically thin (Dickey & Lockman 1990), so we computed the HI column density using the following equation:

$$N_{\text{HI}} = -1.823 \times 10^{18} T_s \int \ln \left[ 1 - \frac{T_B}{T_s - T_{\text{bg}}} \right] dv \quad (3)$$

where  $T_{\text{bg}} \approx 2.66\text{ K}$  is the 21-cm CMB brightness temperature, and  $T_B$  denotes the bright temperature of the HI emission. When  $T_B > T_s - 5\text{ K}$ , it is truncated to this value, with the spin temperature

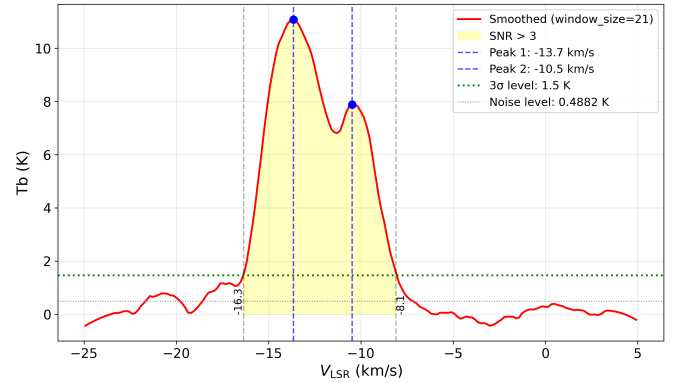


**Figure 2.** The Savitzky-Golay-smoothed <sup>12</sup>CO spectrum at the position of the molecular cloud PGCC G142.03+1.73, with the noise level indicated and the regions with SNR  $> 3$  marked.

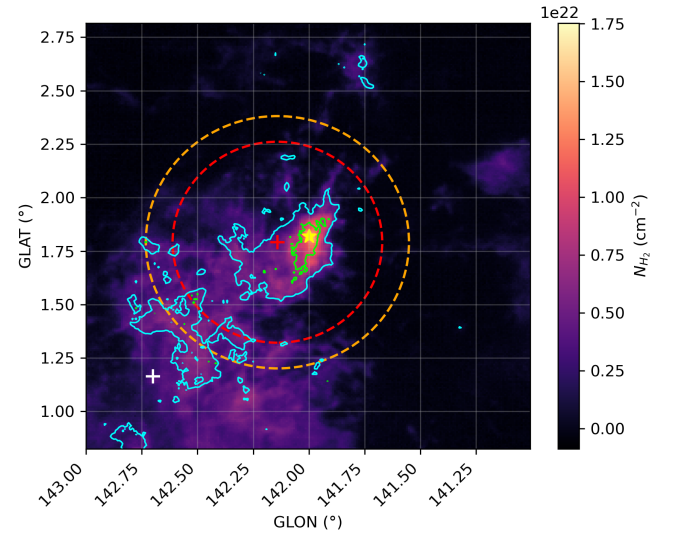


**Figure 3.** Map of the molecular hydrogen column density within the central  $2^\circ \times 2^\circ$  region of interest (ROI). The <sup>13</sup>CO emission contours are outlined in cyan, corresponding to 10% of the peak intensity ( $\sim 3.97\text{ K km/s}$ ), and the C<sup>18</sup>O emission contours are outlined in lime, corresponding to 10% of the peak intensity ( $\sim 0.58\text{ K km/s}$ ). The red cross marks the source center of 4FGL J0330.7+5845e, together with its extension radius (red, dashed circle) and  $ul_{95}$  (orange, dashed circle). The yellow star denotes the protostar AFGL 490, while the white cross marks the source 4FGL J0329.2+5750c.

**Table 2.** The masses for each component, along with the total mass inside the extension radius  $ext = 0.47^\circ$  of source 4FGL J0330.7+5845e.

Component	Mass
H <sub>2</sub>	$8.45 \times 10^3 M_\odot$
HI	$1.71 \times 10^3 M_\odot$
HII	$7.14 \times 10^2 M_\odot$
H <sub>2</sub> + HI + HII	$1.09 \times 10^4 M_\odot$

fixed at  $T_s = 150$  K. From this, we obtained a map of the neutral hydrogen column density within a  $2^\circ \times 2^\circ$  region centered on the ROI and found that the distribution of HI exhibits a diffuse background, showing no significant spatial correlation with the H<sub>2</sub> distribution.

### 3.3 The HII distribution

We used the Planck free-free map (Planck Collaboration et al. 2016a) to obtain the HII density. First, we converted the emission measure (EM) into the free-free intensity using the conversion factor provided in Table 1 of Finkbeiner (2003). We then derived the HII column density from the free-free intensity ( $I_\nu$ ) following Eq. (5) of Sodroski et al. (1997):

$$N_{\text{HII}} = 1.2 \times 10^{15} \text{ cm}^{-2} \left( \frac{T_e}{1 \text{ K}} \right)^{0.35} \left( \frac{\nu}{1 \text{ GHz}} \right)^{0.1} \times \left( \frac{n_e}{1 \text{ cm}^{-3}} \right)^{-1} \frac{I_\nu}{1 \text{ Jy sr}^{-1}}, \quad (4)$$

where  $\nu = 353$  GHz is the frequency, and the electron temperature is  $T_e = 8000$  K. We then adopt an effective electron density of  $2 \text{ cm}^{-3}$ , as suggested by Sodroski et al. (1997) for the region outside the solar circle, to obtain a map of the ionized hydrogen column density within a  $2^\circ \times 2^\circ$  region centered on the ROI. We find that the distribution of ionized hydrogen also exhibits a diffuse morphology and shows no significant spatial correlation with the molecular hydrogen distribution. On the other hand, Simon et al. (1983) previously estimated that an ultra-compact HII region exists at the center of the protostar AFGL 490, but its size is very small ( $\lesssim 0.1''$ ) and therefore does not produce any detectable structure at our observational resolution.

### 3.4 Estimating total proton number density

Firstly, we calculate the total proton mass within the extension radius  $ext = 0.47^\circ$  of source 4FGL J0330.7+5845e by integrating the column densities of three hydrogen species over the source region. The mass of each component is obtained by multiplying its column density by the angular area of the source 4FGL J0330.7+5845e, the square of the distance ( $d = 1$  kpc), and the respective mass per particle. The total proton mass is then given by  $M_p = M_{\text{H}_2} + M_{\text{HI}} + M_{\text{HII}}$ , which represents the total mass of the target material. The derived masses for each component, along with the total mass, are summarized in Tab. 2.

Next, we estimate the size of the molecular cloud within the extension radius using the formula  $R = \sqrt{A/\pi}$ , where  $A$  is the total area of pixels with a molecular hydrogen column density exceeding  $1 \times 10^{21} \text{ cm}^{-2}$ . This yields an estimated radius of  $R \sim 6.5$  pc. With this radius, we model the cloud portion as a uniform sphere, i.e.,  $V = \frac{4}{3}\pi R^3$ , and derive an average proton number density of  $n_p \sim 375 \text{ cm}^{-3}$ .

## 4 THE ORIGIN OF $\gamma$ -RAY EMISSION

To investigate the  $\gamma$ -ray radiation mechanisms in the star-forming region AFGL 490, we fitted the spectral energy distribution (SED) of 4FGL J0330.7+5845e with both leptonic and hadronic models using NAIMA (Zabalza 2015). This computational package provides tools for modeling non-thermal radiation and enables Markov Chain Monte Carlo (MCMC)-based fitting to observational data.

### 4.1 Leptonic scenario

We adopt  $n \sim 375 \text{ cm}^{-3}$  (see Sect. 3.4) as the number density of the target material for relativistic Bremsstrahlung, and then use the following formula (Aharonian 2004) to estimate the cooling timescale:

$$t_{\text{br}} = \frac{\varepsilon_e}{-d\varepsilon_e/dt} \simeq 4 \times 10^7 \left( \frac{n}{1 \text{ cm}^{-3}} \right)^{-1} \text{ yr}. \quad (5)$$

This yields a value of  $t_{\text{br}} \simeq 1.07 \times 10^5$  yr. Furthermore, we tested three electron distribution spectra for relativistic Bremsstrahlung: Power Law (PL), Log-Parabola (LP), and Exponential Cutoff Power Law (ECPL). The Bayesian Information Criterion (BIC) was used for the selection of models (Schwarz 1978), with the results presented in Tab. 3. Ultimately, the ECPL spectrum was adopted for the electron distribution:

$$f(E) = A \left( \frac{E}{E_0} \right)^{-\alpha} \exp \left( -\frac{E}{E_{\text{cutoff}}} \right) \quad (6)$$

where  $E_0 = 1.7$  GeV, the electron spectral index,  $\alpha = 1.6_{-0.4}^{+0.4}$ , and  $E_{\text{cutoff}} = 3.7_{-1.2}^{+2.6}$  GeV. The total electron energy above 3 GeV is  $W_e(>3 \text{ GeV}) = 8.1_{-1.3}^{+1.3} \times 10^{44}$  erg, and above 0.3 GeV it is  $W_e(>0.3 \text{ GeV}) = 3.1_{-0.3}^{+0.3} \times 10^{45}$  erg; the corresponding maximum log-likelihood value for this fit is  $-0.51$ . The relatively large uncertainties in the spectral index and  $E_{\text{cutoff}}$  are likely due to the small number of high-energy photons, which limits the MCMC's ability to constrain these parameters. In addition, although Obonyo et al. (2019) detected non-thermal radio lobes at L-band, the non-detection at C-band means that only an upper limit on the spectral index ( $\alpha_{\text{LC}} < -0.51$  and  $< -0.63$ , respectively) could be inferred. Its usefulness in our modeling is not clear, because our fit is primarily driven by the  $\gamma$ -ray data, and it remains unclear whether the electron population responsible for the non-thermal radio emission is the same (either spatially or energetically) as that produces the  $\gamma$ -ray emission. As a result, the available radio constraint cannot be straightforwardly incorporated to significantly improve the parameter determination. The fitted SED result for relativistic Bremsstrahlung of source 4FGL J0330.7+5845e is shown in Fig. 4.

On the other hand, considering the dense molecular cloud environment within the extension radius of 4FGL J0330.7+5845e and the lack of massive OB stars in this region (see Sect. 1), the UV radiation field is weak, leading to a low photon energy density. Therefore, the efficiency of inverse Compton scattering is expected to be relatively low. Consequently, we disregard the inverse Compton process in our modeling.

### 4.2 Hadronic scenario

As shown in Fig. 3, the  $\gamma$ -ray emission from 4FGL J0330.7+5845e largely encompasses the dense regions of the molecular cloud, as traced by <sup>13</sup>CO and <sup>18</sup>CO. This spatial correspondence provides strong support for a hadronic origin, as the cloud supplies abundant

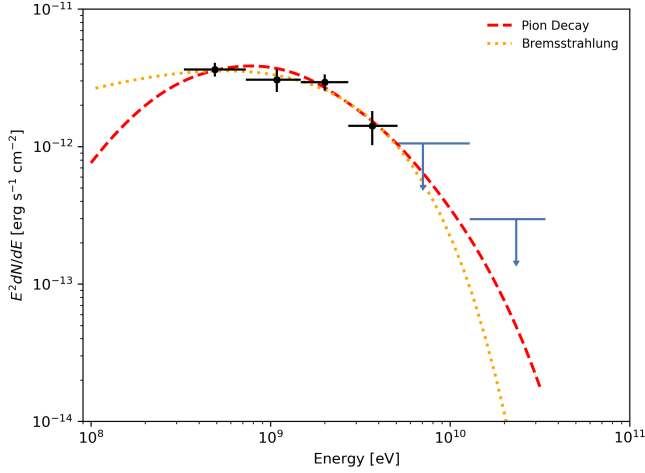


**Figure 4.** The spectral energy distribution (SED) resulting from the  $pp$  interaction process and relativistic Bremsstrahlung of 4FGL J0330.7+5845e, fitted with an exponentially cut-off power-law (ECPL) proton/electron spectrum.

**Table 3.** BIC values for different models.

	PL	LP	ECPL
Bremsstrahlung	15.50	9.12	6.85
PionDecay	11.16	9.64	7.57

target material. We also estimate the cooling time  $t_{pp}$  of relativistic protons due to inelastic  $pp$  interactions by using the following formula (Aharonian 2004):

$$t_{pp} = (n_0 \sigma_{pp} f c)^{-1} \approx 5.3 \times 10^7 \left( \frac{n}{1 \text{ cm}^{-3}} \right)^{-1} \text{ yr}, \quad (7)$$

where we again adopt  $n \sim 375 \text{ cm}^{-3}$  (see Sect. 3.4) and have finally obtained  $t_{pp} \approx 1.41 \times 10^5 \text{ yr}$ .

Similarly, for protons we compared the same three spectral forms: PL, LP, and ECPL. Based on the BIC values shown in Tab. 3, the ECPL spectrum was selected, described by Eq. (6), where  $E_0 = 1.7 \text{ GeV}$ , the proton spectral index is  $\alpha = 1.8^{+0.4}_{-0.5}$ ,  $E_{\text{cutoff}} = 17.1^{+15.6}_{-7.3} \text{ GeV}$ . The total proton energy above 3 GeV is  $W_p(>3 \text{ GeV}) = 2.1^{+0.2}_{-0.2} \times 10^{46} \text{ erg}$ , and above 1 GeV it is  $W_p(>1 \text{ GeV}) = 3.3^{+0.6}_{-0.5} \times 10^{46} \text{ erg}$ ; the corresponding maximum log-likelihood value for this fit is  $-0.86$ . Likewise, the relatively large uncertainties in the spectral index and  $E_{\text{cutoff}}$  are likely due to the limited number of high-energy photons from the source, which weakly constrain the model. Nevertheless, the total proton energy  $W_p$  remains sufficiently well-determined to perform the subsequent energy analysis. The fitted SED result for pion decay of 4FGL J0330.7+5845e is shown in Fig. 4.

## 5 DISCUSSION

We searched for potential  $\gamma$ -ray counterparts within a  $0.5^\circ \times 0.5^\circ$  region centered on the ROI in several catalogs, including SNRcat (Ferrand & Safi-Harb 2012), Green’s Galactic Supernova Remnant Catalog (Green 2019), the ATNF Pulsar Catalog (Lyne et al. 1998), and the WISE AGN Catalog (Assef et al. 2018). No plausible counterpart was identified, so based on positional argument, we consequently

conclude that the source 4FGL J0330.7+5845e is most likely associated with the SF region AFGL 490. In the following, we discuss the two particle acceleration mechanisms mentioned in Sect. 1.

### 5.1 Stellar wind scenario

We employ the following formula to estimate the stellar wind kinetic energy within the cluster core:

$$L_w = \frac{1}{2} \dot{M} v_w^2 = 1 \times 10^{35} \text{ erg s}^{-1} \left( \frac{\dot{M}}{10^{-7} M_\odot \text{ yr}^{-1}} \right) \left( \frac{v_w}{2000 \text{ km s}^{-1}} \right)^2 \quad (8)$$

where  $\dot{M}$  is the mass-loss rate. The mass-loss rate is estimated using the relation  $\dot{M}_{\text{wind}}/\dot{M}_{\text{acc}} \sim 0.1$  (Konigl & Pudritz 2000). (1) For the protostar AFGL 490, an accretion rate of  $\dot{M}_{\text{acc,protostar}} \sim 10^{-5} M_\odot \text{ yr}^{-1}$  (Hsieh et al. 2021) implies a wind mass-loss rate of  $\dot{M}_{\text{wind,protostar}} \sim 10^{-6} M_\odot \text{ yr}^{-1}$ . As the protostar is expected to eventually evolve into a B-type main-sequence star, we adopt a typical B-type main-sequence stellar wind velocity of  $v_{w,\text{protostar}} = 1000 \text{ km s}^{-1}$  (Prinja et al. 1990), which yields a kinetic luminosity of  $L_{w,\text{protostar}} = 2.5 \times 10^{35} \text{ erg s}^{-1}$ . Assuming a protostellar age of  $\sim 10^5 \text{ yr}$ , the total integrated wind energy amounts to  $E_{\text{wind,protostar}} = 7.5 \times 10^{47} \text{ erg}$ . (2) For the other YSOs in the core, we estimate a typical accretion rate of  $\dot{M}_{\text{acc,YSO}} \sim 10^{-8} M_\odot \text{ yr}^{-1}$  per object (Natta et al. 2006), leading to a wind mass-loss rate of  $\dot{M}_{\text{wind,YSO}} \sim 10^{-9} M_\odot \text{ yr}^{-1}$ . We adopt a representative intrinsic wind velocity of  $v_{w,\text{YSO}} = 200 \text{ km s}^{-1}$ . This value is derived from the typical high-velocity component (HVC) of optical forbidden lines in T Tauri stars ( $\sim 100 \text{ km s}^{-1}$ ; Hirth et al. 1997), corrected by a factor of 2 to account for projection effects assuming random spatial orientations (i.e., a mean projection factor of  $\langle \cos i \rangle = 0.5$ ). Consequently, the kinetic luminosity per YSO is  $L_{w,\text{YSO}} = 1 \times 10^{31} \text{ erg s}^{-1}$ . Multiplying by approximately 200 YSOs and an assumed age of  $10^6 \text{ yr}$ , the total wind energy from the low-mass population is  $E_{\text{wind,YSOs}} = 6 \times 10^{46} \text{ erg}$ .

Using the proton energy  $W_p(>3 \text{ GeV}) = 2.1 \times 10^{46} \text{ erg}$  obtained from Sect. 4.2, we calculate the proton acceleration efficiency as  $\eta_p = W_p(>3 \text{ GeV})/(E_{\text{wind,protostar}} + E_{\text{wind,YSOs}}) \approx 2.6\%$ . However, an important point should be noted: if it is assumed that particles are accelerated by the protostar AFGL 490 and the other YSOs separately, the resulting acceleration efficiencies are approximately 2.8% and 35%, respectively. This clearly indicates that, under such a scenario, the stellar wind acceleration from the protostar AFGL 490 overwhelmingly dominates the process.

This derived efficiency appears problematic for several reasons. Firstly, as noted by Romero (2010), the efficiency of particle acceleration by single stellar winds is expected to be very low because of various radiative and adiabatic losses. Furthermore, to date, no isolated massive star has been detected as a  $\gamma$ -ray source powered solely by its wind. Secondly, if we are to compare, the typical acceleration efficiency for supernova remnants (SNRs) is only around 10% (Voelk & Biermann 1988). Moreover, estimates for Young Massive Star Clusters (YMSCs) suggest that the efficiencies of particle acceleration by collective stellar winds are generally below 10%, whilst in some cases it is even lower than 1% (Bykov et al. 2020). Therefore, it remains highly unlikely that the single protostellar wind serves as the primary mechanism for particle acceleration in this source.

## 5.2 Jet scenario

Hsieh et al. (2021) inferred from the Br- $\gamma$  emission line of the protostar AFGL 490 that its accretion luminosity is approximately  $850 L_\odot$ . Then by assuming a ratio of 0.075 between the jet kinetic luminosity and the accretion luminosity (Cabrit 2007), the kinetic luminosity of the protostar AFGL 490 jet is estimated to be  $L_j = 2.44 \times 10^{35} \text{ erg s}^{-1}$ . Next, we estimate the time required to accelerate protons up to the necessary energy to produce the observed  $\gamma$ -ray emission by using the following equation:

$$t_{\text{injection}} = \frac{W_p}{\eta L_j} \quad (9)$$

where  $W_p$  is the total proton energy (see Sect. 4.2),  $\eta$  is the proton acceleration efficiency of the jet, which we vary between 2% and 10% (Araudo et al. 2021), and  $L_j$  is the jet kinetic luminosity. The resulting acceleration time ranges from  $10^4$  to  $10^5$  years. This range is consistent with the estimated age of the protostar AFGL 490 ( $10^4$ – $10^5$  years) and is also comparable to the estimated lifetime of  $4 \times 10^4$  years for the HH 80-81 protostellar jet (Qiu et al. 2019). Furthermore, this acceleration timescale falls within the same order of magnitude as the two cooling timescales ( $t_{\text{br}}$  and  $t_{\text{pp}}$ ) estimated in Sect. 4.

On the other hand, we also estimate the maximum charge energy achievable by the protostellar jet of AFGL 490 using the following relation (Wang et al. 2025):

$$L_j \geq 10^{38} \left( \frac{E_{\text{max}}}{10 \text{ PeV}} \right)^2 \tilde{\omega} \beta^{-1} \sigma_{-1}^{-1} \text{ erg s}^{-1} \quad (10)$$

where  $L_j$  is the kinetic luminosity of the jet,  $E_{\text{max}}$  is the maximum energy of charged particles,  $\tilde{\omega}$  is a jet geometry factor assumed to be 1 for a collimated jet, and  $\beta$  is the maximum bulk velocity of the jet, for which we adopt a value of  $\beta \approx 0.0033$  (corresponding to  $v = 1000 \text{ km/s}$ ). The parameter  $\sigma = B^2 / (2\pi\rho v^2)$  is the non-relativistic magnetization parameter, where  $\sigma_{-1} = \sigma / 0.1$ . For our calculation, we assume a mean magnetic field strength  $B = 0.1 \text{ mG}$  (Rodríguez-Kamenetzky et al. 2019; Méndez-Gallego et al. 2025) and a jet particle density  $n_j = 10^4 \text{ cm}^{-3}$  (Araudo et al. 2021), with  $v = \beta c$ .

For a jet with a kinetic luminosity of  $L_j = 2.44 \times 10^{35} \text{ erg s}^{-1}$ , our calculation yields a maximum energy of charged particles of  $E_{\text{max}} \approx 0.09 \text{ TeV}$ . This result is consistent with the typical maximum proton energy of 0.24 TeV predicted for acceleration in protostellar jets by Araudo et al. (2021). And for our ECPL proton/electron distribution model, we define the maximum proton/electron energy  $E_{\text{max}}$  as the energy containing 99.99% of the total distribution. This yields  $E_{p,\text{max}} = 78.4 \text{ GeV}$  and  $E_{e,\text{max}} = 23.6 \text{ GeV}$ . Both values lie comfortably within the acceleration limit derived above.

## 5.3 Diffusion of high-energy particles

We use the following two expressions to calculate the diffusion radius of high-energy protons and electrons in the molecular cloud, respectively (Aharonian 2004):

$$R_{\text{diff,p}}(E, t) = 2\sqrt{D(E)t \frac{e^{t\delta/t_{\text{pp}}} - 1}{t\delta/t_{\text{pp}}}}, \quad (11)$$

and

$$R_{\text{diff,e}}(E, t) \approx 2\sqrt{D(E)t \frac{1 - (1 - E/E_{\text{cut}})^{1-\delta}}{(1-\delta)E/E_{\text{cut}}}}. \quad (12)$$

Here the diffusion coefficient is defined as  $D(E) = D_0 (E/10 \text{ GeV})^\delta$ , where  $D_0$  typically lies in the range  $10^{26}$ – $10^{28} \text{ cm}^2 \text{ s}^{-1}$ . In this work, we adopt  $D_0 = 10^{26} \text{ cm}^2 \text{ s}^{-1}$ , which

**Table 4.** The ranges of diffusion radius (in units of pc) for particles with different energies, for diffusion times ranging from  $10^4$  to  $10^5$  yr.

Energy	3GeV	10GeV	78.7GeV
$R_{\text{diff,p}}(\text{pc})$	2.7 - 9.3	3.7 - 12.6	6.2 - 21.1
Energy	3GeV	10GeV	21.2GeV
$R_{\text{diff,e}}(\text{pc})$	2.7 - 8.5	3.6 - 11.5	4.4 - 13.9

represents a denser environment, to obtain a lower limit on the diffusion radius, and set  $\delta = 0.5$ . The diffusion time is taken to be  $t = 10^4$ – $10^5$  yr.

For Eq. (11), we adopt the proton–proton interaction timescale  $t_{\text{pp}} \approx 1.41 \times 10^5$  yr, as derived in Sect. 4.2 and in Eq. (12), the time-dependent cutoff energy is given by  $E_{\text{cut}}(t) \approx m_e c^2 / [(7 \times 10^{-20} \text{ eV cm}^{-3} \text{ s}^{-1}) t]$ . The resulting diffusion radius for different particle energies are listed in Tab. 4. Considering that the characteristic size of the molecular cloud derived in Sect. 3.4 is  $R \sim 6.5 \text{ pc}$ , and that the physical scale of the 4FGL J0330.7+5845e is  $\sim 8.2 \text{ pc}$ , as derived from the  $\text{ext} = 0.47^\circ$ , it is therefore plausible that these high-energy particles can diffuse within the cloud and produce the observed extended  $\gamma$ -ray source, 4FGL J0330.7+5845e.

## 6 CONCLUSION

In this paper, we report the detection of GeV  $\gamma$ -ray emission toward the star-forming region AFGL 490. Through a relocalization of the source 4FGL J0330.7+5845, we have identified a significantly extended source, which is designated 4FGL J0330.7+5845e. The emission is well-modeled by a Gaussian spatial template with an extension radius of  $0.47^\circ$  and a high test statistic ( $\text{TS} = 172$ ). The centroid of this extended emission is located  $0.144^\circ$  from the protostar AFGL 490, a separation that lies well within the 95% containment radius ( $r_{95} = 0.147^\circ$ ). The source exhibits significant spatial extension across multiple energy ranges, including 0.3–300 GeV, 0.3–1 GeV, and 1–300 GeV, with  $\text{TS}_{\text{ext}} > 16$  in all cases, and its spectral energy distribution is fit by a log-parabolic function with notable curvature, indicative of a high-energy cutoff ( $\alpha = 2.312 \pm 0.112$ ,  $\beta = 0.234 \pm 0.089$ ,  $E_b = 1038 \text{ MeV}$ ).

Our investigation, which combines an analysis of the ambient gas distribution with theoretical modeling, does not allow us to unambiguously determine whether the leptonic or hadronic channel dominates the observed emission. In the absence of compelling alternative candidates, however, the protostellar jet of AFGL 490 remains a plausible acceleration scenario capable of accounting for the observed gamma-ray emission.

Future observations with next-generation telescopes, offering superior angular resolution, will be pivotal in revealing any potential fine-scale structure or additional point sources within this complex region. Furthermore, multi-wavelength campaigns, combining data across different bands, will be essential to place more stringent constraints on the physical parameters of the protostellar jet and to further elucidate the particle acceleration processes at work.

## ACKNOWLEDGEMENTS

This work is supported by the National Natural Science Foundation of China (NSFC) grant 12273122, National Astronomical Data Center, the Greater Bay Area, under grant No. 2024B1212080003, and science research grant from the China Manned Space Project under CMS-CSST-2025-A13. This research made use of the data from the

Milky Way Imaging Scroll Painting (MWISP) project, which is a multi-line survey in  $^{12}\text{CO}/^{13}\text{CO}/\text{C}^{18}\text{O}$  along the northern galactic plane with PMO-13.7m telescope. We are grateful to all the members of the MWISP working group, particularly the staff members at PMO-13.7m telescope, for their long-term support. MWISP was sponsored by National Key R&D Program of China with grants 2023YFA1608000 & 2017YFA0402701 and by CAS Key Research Program of Frontier Sciences with grant QYZDJ-SSW-SLH047.

## DATA AVAILABILITY

The Fermi-LAT data used in this work are publicly available, and are provided online at the NASA-GSFC Fermi Science Support Center<sup>3</sup>. We made use of the CO data from the MWISP<sup>4</sup> to study the distribution of  $\text{H}_2$ , and the HII and HI data are taken from Planck legacy archive<sup>5</sup> and HI4PI<sup>6</sup>, respectively.

## REFERENCES

- Abdollahi S., et al., 2022, *ApJS*, **260**, 53
- Abeyssekara A. U., et al., 2021, *Nature Astronomy*, **5**, 465
- Ackermann M., et al., 2011, *Science*, **334**, 1103
- Aharonian F. A., 2004, Very high energy cosmic gamma radiation : a crucial window on the extreme Universe, doi:10.1142/4657.
- Akaike H., 1974, *IEEE Transactions on Automatic Control*, **19**, 716
- Araudo A. T., Romero G. E., Bosch-Ramon V., Paredes J. M., 2007, *A&A*, **476**, 1289
- Araudo A. T., Padovani M., Marcowith A., 2021, *MNRAS*, **504**, 2405
- Assef R. J., Stern D., Noirot G., Jun H. D., Cutri R. M., Eisenhardt P. R. M., 2018, *ApJS*, **234**, 23
- Ballet J., Bruel P., Burnett T. H., Lott B., The Fermi-LAT collaboration 2023, *arXiv e-prints*, p. arXiv:2307.12546
- Bell A. R., 1978, *MNRAS*, **182**, 147
- Blandford R. D., Ostriker J. P., 1978, *ApJ*, **221**, L29
- Bolato A. D., Wolfire M., Leroy A. K., 2013, *ARA&A*, **51**, 207
- Bosch-Ramon V., Romero G. E., Araudo A. T., Paredes J. M., 2010, *A&A*, **511**, A8
- Bykov A. M., Gladilin P. E., Osipov S. M., 2013, *MNRAS*, **429**, 2755
- Bykov A. M., Marcowith A., Amato E., Kalyashova M. E., Kruijssen J. M. D., Waxman E., 2020, *Space Sci. Rev.*, **216**, 42
- Cabrit S., 2007, in Ferreira J., Dougados C., Whelan E., eds., Vol. 723, *Lecture Notes in Physics*, Berlin Springer Verlag. p. 21
- Dame T. M., Hartmann D., Thaddeus P., 2001, *ApJ*, **547**, 792
- Dickey J. M., Lockman F. J., 1990, *ARA&A*, **28**, 215
- Ferrand G., Safi-Harb S., 2012, *Advances in Space Research*, **49**, 1313
- Finkbeiner D. P., 2003, *ApJS*, **146**, 407
- Ge T.-T., Sun X.-N., Yang R.-Z., Tam P.-H. T., Lu M.-X., Liang E.-W., 2024, *MNRAS*, **530**, 1144
- Green D. A., 2019, *Journal of Astrophysics and Astronomy*, **40**, 36
- HI4PI Collaboration et al., 2016, *A&A*, **594**, A116
- Hirth G. A., Mundt R., Solf J., 1997, *A&AS*, **126**, 437
- Hsieh T.-H., et al., 2021, *ApJ*, **912**, 108
- Konigl A., Pudritz R. E., 2000, in Mannings V., Boss A. P., Russell S. S., eds, *Protostars and Planets IV*. p. 759 (arXiv:astro-ph/9903168), doi:10.48550/arXiv.astro-ph/9903168
- Kulkarni S., Desai S., 2017, *Ap&SS*, **362**, 70
- Lhaaso Collaboration 2024, *Science Bulletin*, **69**, 449
- Lhaaso Collaboration et al., 2025, *Science China Physics, Mechanics, and Astronomy*, **68**, 279503
- Liddle A. R., 2007, *Monthly Notices of the Royal Astronomical Society: Letters*, **377**, L74
- Lucy L. B., Solomon P. M., 1970, *ApJ*, **159**, 879
- Lyne A. G., et al., 1998, *MNRAS*, **295**, 743
- Masiunas L. C., Gutermuth R. A., Pipher J. L., Megeath S. T., Myers P. C., Allen L. E., Kirk H. M., Fazio G. G., 2012, *ApJ*, **752**, 127
- Méndez-Gallego J., López-Coto R., de Oña Wilhelmi E., Fedriani R., Otero-Santos J., Cantürk Y., 2025, *A&A*, **695**, A11
- Morlino G., Blasi P., Peretti E., Cristofari P., 2021, *MNRAS*, **504**, 6096
- Natta A., Testi L., Randich S., 2006, *A&A*, **452**, 245
- Navarete F., Daminieli A., Barbosa C. L., Blum R. D., 2015, *MNRAS*, **450**, 4364
- Obonyo W. O., Lumsden S. L., Hoare M. G., Purser S. J. D., Kurtz S. E., Johnston K. G., 2019, *MNRAS*, **486**, 3664
- Planck Collaboration et al., 2016a, *A&A*, **594**, A10
- Planck Collaboration et al., 2016b, *A&A*, **594**, A28
- Prinja R. K., Barlow M. J., Howarth I. D., 1990, *ApJ*, **361**, 607
- Qiu K., Wyrowski F., Menten K., Zhang Q., Güsten R., 2019, *ApJ*, **871**, 141
- Reid M. J., et al., 2019, *ApJ*, **885**, 131
- Rodríguez-Kamenetzky A., Carrasco-González C., González-Martín O., Araudo A. T., Rodríguez L. F., Vig S., Hofner P., 2019, *MNRAS*, **482**, 4687
- Romero G. E., 2010, *Mem. Soc. Astron. Italiana*, **81**, 181
- Savitzky A., Golay M. J. E., 1964, *Analytical Chemistry*, **36**, 1627
- Schreyer K., Henning T., van der Tak F. F. S., Boonman A. M. S., van Dishoeck E. F., 2002, *A&A*, **394**, 561
- Schreyer K., Semenov D., Henning T., Forbrich J., 2006, *ApJ*, **637**, L129
- Schwarz G., 1978, *Annals of Statistics*, **6**, 461
- Simon M., Felli M., Cassar L., Fischer J., Massi M., 1983, *ApJ*, **266**, 623
- Snell R. L., Scoville N. Z., Sanders D. B., Erickson N. R., 1984, *ApJ*, **284**, 176
- Sodroski T. J., Odegard N., Arendt R. G., Dwek E., Weiland J. L., Hauser M. G., Kelsall T., 1997, *ApJ*, **480**, 173
- Straižys V., Laugalys V., 2008, in Reipurth B., ed., Vol. 4, *Handbook of Star Forming Regions*, Volume I. p. 294, doi:10.48550/arXiv.0811.2992
- Su Y., et al., 2019, *ApJS*, **240**, 9
- Sun X.-N., Yang R.-Z., Liang Y.-F., Peng F.-K., Zhang H.-M., Wang X.-Y., Aharonian F., 2020, *A&A*, **639**, A80
- Voelk H. J., Biermann P. L., 1988, *ApJ*, **333**, L65
- Wang J., Reville B., Aharonian F. A., 2025, *ApJ*, **989**, L25
- Wenger M., et al., 2000, *A&AS*, **143**, 9
- Wood M., Caputo R., Charles E., Di Mauro M., Magill J., Perkins J. S., Fermi-LAT Collaboration 2017, in 35th International Cosmic Ray Conference (ICRC2017). p. 824 (arXiv:1707.09551), doi:10.22323/1.301.0824
- Yan D.-H., Zhou J.-N., Zhang P.-F., 2022, *Research in Astronomy and Astrophysics*, **22**, 025016
- Yang R.-z., Aharonian F., 2017, *A&A*, **600**, A107
- Yang R.-Z., Wang Y., 2020, *A&A*, **640**, A60
- Yang R.-z., de Oña Wilhelmi E., Aharonian F., 2018, *A&A*, **611**, A77
- Zabalza V., 2015, in 34th International Cosmic Ray Conference (ICRC2015). p. 922 (arXiv:1509.03319), doi:10.22323/1.236.0922
- de Oña Wilhelmi E., López-Coto R., Su Y., 2023, *MNRAS*, **523**, 105

This paper has been typeset from a  $\text{\TeX}/\text{\LaTeX}$  file prepared by the author.

<sup>3</sup> <https://fermi.gsfc.nasa.gov/ssc/data/access/lat/>

<sup>4</sup> <http://www.dlh.pmo.cas.cn/ENGLISH/MWISP/>

<sup>5</sup> <https://pla.esac.esa.int/pla/#home>

<sup>6</sup> <https://cdsarc.u-strasbg.fr/viz-bin/qcat?J/A+A/594/A116>